



Dual-band *in situ* molecular spectroscopy using single-sized Al-disk perfect absorbers

| | |
|-------------------------------|--|
| Journal: | <i>Nanoscale</i> |
| Manuscript ID | NR-ART-01-2019-000904.R1 |
| Article Type: | Paper |
| Date Submitted by the Author: | 01-Apr-2019 |
| Complete List of Authors: | Dao, Thang; National Institute for Materials Science International Center for Materials Nanoarchitectonics Chen, Kai; National Institute for Materials Science International Center for Materials Nanoarchitectonics; Jinan University NAGAO, Tadaaki; National Institute for Materials Science International Center for Materials Nanoarchitectonics; Hokkaido University |
| | |

Dual-band *in situ* molecular spectroscopy using single-sized Al-disk perfect absorbers†

Thang Duy Dao,^{*a} Kai Chen^{ab} and Tadaaki Nagao^{*ac}

Received 00th January 20xx,
Accepted 00th January 20xx

DOI: 10.1039/x0xx00000x

We propose antenna-enhanced infrared vibrational spectroscopy by adopting single-sized Al disks on Al₂O₃-Al films fabricated by colloidal-mask lithography. The precisely designed plasmonic resonator with dual-band perfect absorption (DPA) shows strongly-enhanced nearfield intensity and polarization independence, at both resonances, providing a powerful antenna platform for the multi-band vibrational sensing. As a proof of concept, we experimentally apply the plasmonic DPAs in bond-selective dual-band infrared sensing of an ultrathin polydimethylsiloxane (PDMS) film, simultaneously amplifying two representative vibrational bands (asymmetric C-H stretching of CH₃ at 2962 cm⁻¹ and CH₃ deformation of Si-CH₃ at 1263 cm⁻¹) by surface-enhanced infrared absorption spectroscopy (SEIRA). The plasmonic DPA was successfully adopted for the *in situ* monitoring of reaction kinetics, by recording the spectral changes in C-H stretching and Si-CH₃ deformation modes of a 10-nm PDMS elastomer, which are selectively enhanced by the two antenna resonances, during its gelation process. Our systematic study of the SEIRA spectra has demonstrated mode splitting and a clear avoided-crossing in the dispersion curve as a function of resonance frequency of DPA, manifesting itself as a promising basis for future polaritonic devices utilizing the hybridization between the molecular vibrational states and the enhanced light field.

Introduction

Engineering of efficient light absorption and nearfield enhancement at desired wavelengths by metamaterial perfect absorbers (PAs) provides us a wide variety of applications that would be impossible using natural materials. Since the first PA was experimentally realized by Landy *et al.* in 2008 in the gigahertz frequency region¹, the concept of the PA has enjoyed its widespread applicability from the terahertz and infrared (IR), to the visible spectral regions owing to its unique ability to achieve 100% absorptance, or unity absorptivity. In the past decade, PAs have attracted much attention in the IR spectral range owing to their significant impact on thermal devices and IR spectroscopy applications, such as in thermal emitters^{2–7}, IR detectors^{8–13}, gas sensing^{14,15}, thermophotovoltaic^{16–19} and radiative cooling^{20–23}, and especially in surface-enhanced infrared absorption spectroscopy (SEIRA)^{24–33}. Most structural

designs for PAs have focused on the controllability and tunability of their resonant frequency, bandwidth, polarization, and working angle as well as their reconfigurability. In this regard, increasing demand exists not only on single-band PAs, but also on dual- and multiple-band PAs due to their great potential in non-destructive chemical analysis and in remote sensing applications such as non-dispersive infrared spectroscopy (NDIR)¹⁴, particularly in simultaneous multiple-band SEIRA^{29,32}.

Among those dual-band perfect absorbers (DPAs) designs, many structures have been proposed, including patterned symmetric cross-shapes arrays^{5,34,35}, asymmetric cross-shape arrays²⁹, elliptical nanodisk arrays³⁶, two different nanopatterns^{14,32,37}, T-shaped plasmonic arrays³⁸, and distinct dielectric spacing layers³⁹. These structures rely on the first order of the magnetic resonances within two different resonators simultaneously arranged in the top layers; and they have been successfully applied for NDIR¹⁴ and SEIRA^{29,32} applications. Another approach to achieve dual- or multiple-band resonances is to utilize the second⁴⁰ or third^{41–43} orders of the fundamental magnetic modes in plasmonic metal PAs. These DPAs can be realized with single-sized building block structures, which can exhibit polarization-independent resonances with a wide working angle, as well as high tunability. In addition, with nearly perfect absorption and strong nearfield enhancement at the resonances, the DPA based on the single-sized resonator array can be also a desirable IR plasmonic platform for enhancing light-matter interactions, especially for simultaneous dual-band vibrational sensing as well as real-time observation of molecular reaction kinetics.

^a International Center for Materials Nanoarchitectonics, National Institute for Materials Science (NIMS), 1-1 Namiki, Tsukuba, Ibaraki 305-0044, Japan. Emails: Dao.Duythang@nims.go.jp; Nagao.Tadaaki@nims.go.jp

^b Institute of Photonics Technology, Jinan University, Guangzhou, 510632, China.

^c Department of Condensed Matter Physics, Graduate School of Science, Hokkaido University, Kita 8, Nishi 5, Kita-ku, Sapporo 060-0810, Japan.

†Electronic Supplementary Information (ESI) available: Electronic supplementary information (ESI) available: Additional optical properties of the DPAs (further numerical optimization of structural parameters of DPAs; derivation of SPP in the plasmonic hexagonal lattice and its coupling to the third-order magnetic resonance; measured polarization independence of the absorptivity spectra of samples S3 and S4); spectroscopic ellipsometry study of the PDMS film; detailed calculations of the SEIRA enhancement factors; further analysis of curing dynamics of PDMS by SEIRA; angle-resolved SEIRA study; detailed optical properties of samples S6 and S7; further SEIRA analysis at the M1 resonance and the retrieved permittivity table for PDMS. See DOI: 10.1039/x0xx00000x

In this work, we demonstrate dual-band perfect absorbers (DPAs) with high tunability in the mid-infrared (MIR) region for effective use in detecting a trace amount of molecules as well as in monitoring their reaction processes. The structural design of the DPAs comprises an array of single-sized symmetric Al disk resonators fabricated by colloidal-mask lithography and a metal-insulator bilayer placed beneath them. This design has multiple advantages over the previous dual-band SEIRA devices^{29,32} using two different resonators made of Au, fabricated by electron-beam lithography. The DPAs were designed by high-precision numerical electromagnetic simulations which adopts both the surface plasmon polariton (SPP)-coupled (third-order) magnetic resonance and the fundamental magnetic resonance. Remarkably, the proposed plasmonic DPAs exhibited excellent absorptivity (i.e. 98%), with polarization independence at both resonances. Furthermore, with wide tunability in the mid-IR region, the resonances of DPAs' span the majority of the molecular fingerprint region. With strong nearfield coupling and confinement in the subwavelength plasmonic cavity, the fabricated DPAs showed exceptional success as IR plasmonic antennas for the multispectral SEIRA spectroscopy. We exemplified the wavelength-selective SEIRA detection capability using the plasmonic DPAs to simultaneously enhance two vibrational bands (asymmetric C-H stretching in CH₃ at 2962 cm⁻¹ and CH₃ deformation in Si-CH₃ at 1263 cm⁻¹) of a 10-nm

polydimethylsiloxane (PDMS) film. In particular, we successfully applied our DPA antennas to the *in situ* monitoring of the gelation process and reaction kinetics of a 10-nm PDMS film. Our further analyses revealed Fano coupling between the molecular vibrations and the antenna resonance as evidenced by the remarkable mode splitting and anti-crossing in the polaritonic bands. The obtained knowledge here can serve as a promising basis for the polariton-based mid-infrared devices based on the hybridization between the vibrational states of matter and plasmonic excitations.

Results and discussion

Structure and optical properties of the DPAs

Fig. 1a illustrates a schematic design of the DPA with periodicity p , disk diameter d , and insulating layer thickness t as geometrical parameters. In this work, the Al film is fixed at 0.1 μm while the thickness of the Al disks is optimized at 0.1 μm (Fig. S1a†). Therefore, the optical properties of the DPA are mainly controlled by changing p , d and t . The inset in Fig. 1a depicts the reciprocal lattice space (momentum space) of the upper Al disk hexagonal array, where the lattice constant k is transformed from the corresponding real space lattice constant ($k = \frac{4\pi}{\sqrt{3}p}$). Fig. 1b presents the simulated

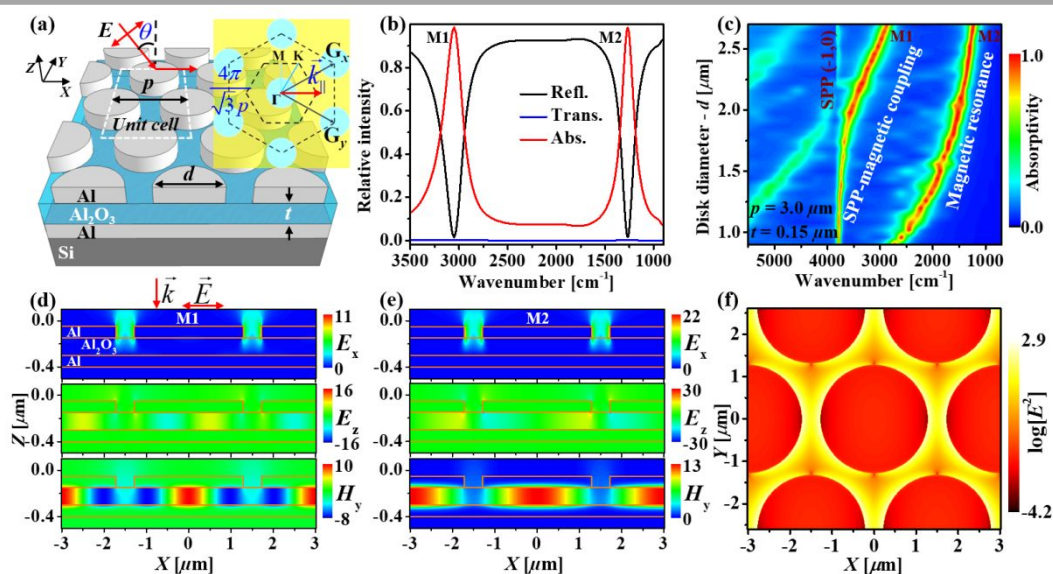


Fig. 1. (a) A schematic illustration of DPAs with definition of a simulation unit cell (dashed rectangle) and geometrical parameters: periodicity p , Al disk diameter d and insulating Al_2O_3 thickness t . The inset in (a) describes a reciprocal lattice of the top Al disk array with a lattice constant of $\frac{4\pi}{\sqrt{3}p}$. (b) Simulated spectra of a DPA ($p = 3.0 \mu\text{m}$, $d = 2.55 \mu\text{m}$, $t = 0.15 \mu\text{m}$, Al disks and bottom film of 0.1 μm thick) manifest two perfect absorption peaks at 3044 cm⁻¹ (M1) and 1280 cm⁻¹ (M2). (c) Simulated absorptivity of DPAs with different disk diameters (fixed p and t at 3.0 μm and 0.15 μm , respectively) shows the tunability of DPAs covering the MIR region. (d) – (e) Electric fields (E_x , top), (E_z , middle) and magnetic field (H_y , bottom) distributions in a DPA ($p = 3.0 \mu\text{m}$, $d = 2.55 \mu\text{m}$, and $t = 0.15 \mu\text{m}$) excited at both M1 (d) and M2 (e) resonances shown in (b). (f) Simulated total electric field intensity distribution (plotted in decimal log scale) in the X - Y plane at M2 evidences strongly enhanced nearfield at vicinity of Al disks. In the simulations, the incident electric field propagated along the $-Z$ -direction (at normal incidence) and oscillated along the X -axis; the intensity spectra were taken at normal angle; the incident fields amplitudes were normalized to unity.

transmittance, reflectance, and absorptivity spectra at normal incidence of a DPA with $p = 3.0 \mu\text{m}$, $d = 2.55 \mu\text{m}$, $t = 0.15 \mu\text{m}$ (optimized thickness for $3.0\text{-}\mu\text{m}$ periodicity DPAs, see Fig. S1b†). As seen in Fig. 1b, the DPA exhibits a pair of narrow absorption bands resonating at 3044 cm^{-1} (M1) and 1280 cm^{-1} (M2) with nearly perfect absorptivity (0.98). It has been shown that in a metal-insulator-metal dipole absorber, the induced electric dipole at the lower metal film oscillates with opposite phase compared to that of the electric dipole in the upper metallic resonator, resulting in an enhancement of the magnetic field between the upper and the lower metals layers. This resonance is therefore called the magnetic resonance. In addition to the fundamental magnetic resonance (the smaller wavenumber resonance, namely M2), an additional absorption band is observed in the higher wavenumber range, which is the SPP-coupled magnetic resonance resulting from hybridization between the third-order magnetic resonance and the photonic mode (SPP) of the periodic Al disk array (the higher wavenumber resonance, namely M1).

To further understand the origin of these two resonant bands, we performed an angle-resolved simulation (plotted in wavelength). The result is shown in Fig. S2a†. It was found that, for the fundamental magnetic mode, M2 (the longer-wavelength or lower-wavenumber resonance), the resonant peak position and peak intensity is almost unchanged across a wide incident angle range up to 80° ($^\circ$). By contrast, as a result of SPP-coupling with the magnetic resonance, the shorter-wavelength resonance (higher wavenumber), M1, changes dramatically when the incident angle increases beyond 15° : in addition, it strongly depends on the periodicity of the hexagonal lattice (Fig. S2b†). In a plasmonic hexagonal lattice, SPPs at the metal-air interface are excited if their momentum matches the momentum of the incident photon and the hexagonal lattice. At normal incidence, the resonant SPP wavelength

is calculated using the expression $\lambda_{\text{spp}} = \frac{\sqrt{3}p}{2\sqrt{(i^2 + ij + j^2)}} \sqrt{\frac{\epsilon_m}{\epsilon_m + 1}}$ (see

the ESI† for the detailed derivation). Here, with $p = 3.0 \mu\text{m}$, the SPP resonance is found at $2.6 \mu\text{m}$ (3846 cm^{-1}). As shown in Fig. S2†, M1 is clearly originated from the coupling between the SPP mode (-1,0) (dashed black curves) and the third-order magnetic resonance. By tuning the size of Al disk, both resonant bands are readily tuned in the MIR region to span the most interesting range of molecular vibrations (Fig. 1c and Fig. S2c†). Here we used the half-wave dipole antenna model to exemplify the dependence of the resonance of the DPA on the diameter of the Al disk and to estimate the coupling energy strength (i.e. 28 meV) between the SPP and the third-order magnetic resonance (see details in the ESI†). The electromagnetic field distribution was also simulated on the resonances to confirm the optical properties of the DPA. As shown in Fig. 1d – Fig. 1f, the electric fields (E_z) excited at both M1 and M2 display opposite phase oscillations at the upper Al disk and the lower Al film, resulting in dramatic enhancement of magnetic field (i.e. 10 times). As stated above, M1 originates from the third-order magnetic resonance coupled with the SPP and the electric field distribution for this resonance clearly shows three spots of the enhanced resonant magnetic field below each resonator (Fig. 1d) while M2, which results

from the fundamental magnetic resonance, exhibits only one spots of the enhanced resonant magnetic field (Fig. 1e). Furthermore, the total electric field intensity distribution in the X-Y plane taken at the interface between the Al disks array and Al_2O_3 layer (Fig. 1f, see Fig. S3† for the detailed E_x and E_z distributions) indicates strong nearfield intensity enhancement (i.e. 1000 times), suggesting that the DPA can be a good antenna platform for nearfield-enhanced spectroscopy applications such as SEIRA, especially for dual-band SEIRA utilizing both the M1 and M2 resonances.

Large-area fabricated DPAs

To realize the DPA structure (i.e. $1 \times 1 \text{ cm}^2$ as shown in the inset of Fig. 2a), we employed a colloidal-mask lithography process involving two reactive-ion etching (RIE) steps⁶. The details are shown in the Methods section. Here, a set of five DPAs with the same periodicity and insulator thickness ($p = 3.0 \mu\text{m}$, and $t = 0.15 \mu\text{m}$) but different diameters were numerically simulated and precisely fabricated (SEM images, Fig. 2, upper row of images), namely, S1 ($d = 2.08 \mu\text{m}$, Fig. 2a), S2 ($d = 2.21 \mu\text{m}$, Fig. 2b), S3 ($d = 2.32 \mu\text{m}$, Fig. 2c), S4 ($d = 2.43 \mu\text{m}$, Fig. 2d) and S5 ($d = 2.55 \mu\text{m}$, Fig. 2e). The absorptivity spectra of the fabricated DPAs were measured using a Fourier-transform infrared (FTIR) spectrometer equipped with a reflection compartment accessory. Fig. 2, from top to bottom, presents the SEM images, and the simulated and measured absorptivity spectra of the five DPAs, respectively. Typical SEM images obtained for each sample indicate the well-defined periodic structures. Using this scalable colloidal-mask lithography technique, the obtained domain size of the Al disk lattice was from a few tens to a few hundreds of unit cells, which agrees well with the infinite periodic lattice model used in the simulation. As seen in Fig. 2, the measured results agree well with the simulated spectra. All five fabricated DPAs reveal two narrow resonances (the quality factor $-Q \approx 13$ for M1 resonant modes, $Q \approx 9$ for M2 resonant modes) with high absorptivities (0.86 – 0.93 for the M1 modes, 0.94 – 0.98 for the M2 modes). The Q factors of M1 resonant modes are higher than those of the M2 modes in all five fabricated DPAs because the M1 resonance results from the grating-mediated coupling between the SPP and the third-order magnetic resonance. The resonant peak positions of M1 modes and M2 modes of the DPAs are redshifted with increasing the diameter of the Al disk. The wavenumbers of the M1 resonance decreases from 3470 cm^{-1} (S1) to 3360 cm^{-1} (S2), 3280 cm^{-1} (S3), 3220 cm^{-1} (S4) and to 3044 cm^{-1} (S5) with high absorptivities ranging from 0.86 (S1) to 0.93 (S5). Similarly, the wavenumbers of M2 resonance also decreases with increasing the disk diameter, from 1484 cm^{-1} (S1) to 1410 cm^{-1} (S2), 1370 cm^{-1} (S3), 1326 cm^{-1} (S4) and to 1280 cm^{-1} (S5) with excellent absorptivities from 0.94 (S1) to 0.98 (S5). Interestingly, with a symmetrical geometry, both resonant peaks of the DPAs are polarization-independent at normal incidence. Indeed, Fig. S4a† and Fig. S4b† display the simulated and measured polarization-independent absorptivity maps for S5. The measured polarization-independent absorptivity maps of S3 and S4 are also provided in Fig. S4c† and Fig. S4d†, respectively. The peak positions and intensities of M1 and M2 stay almost unchanged when the

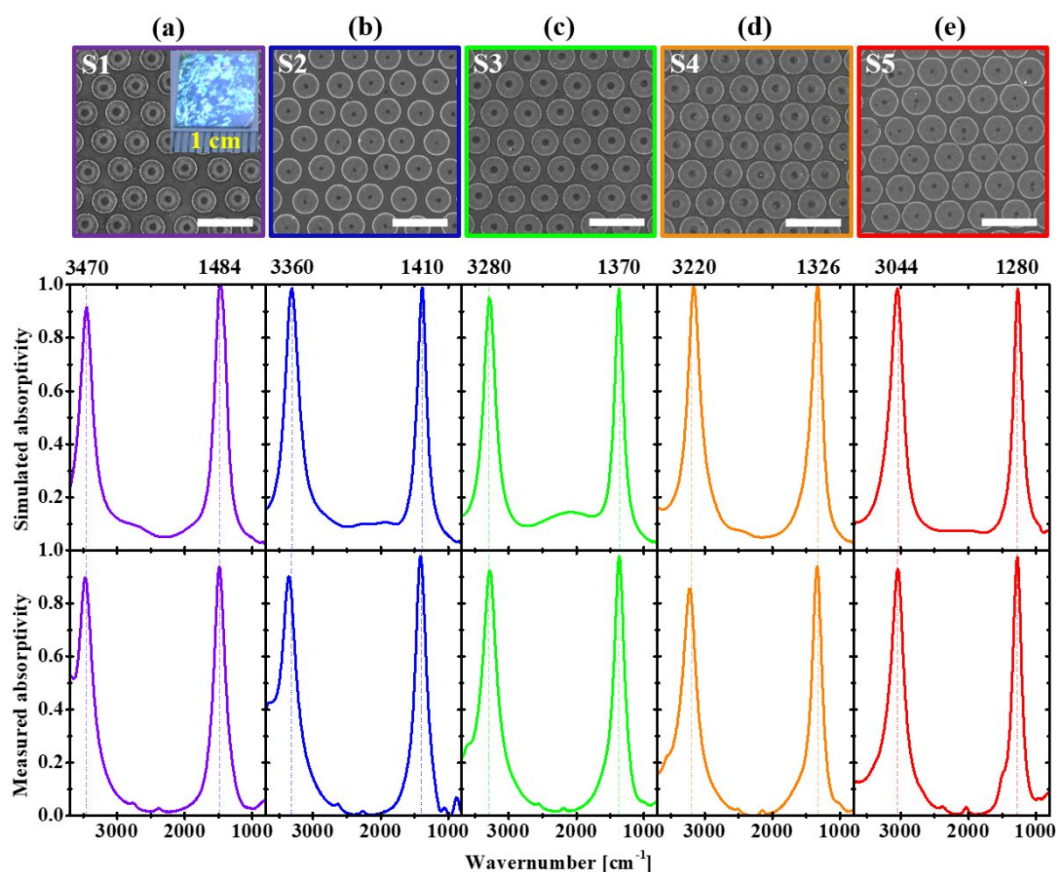


Fig. 2. From top to bottom: SEM images, simulated and measured absorptivity spectra of five different DPAs having the same periodicity and insulator thickness ($p = 3.0 \mu\text{m}$, $t = 0.15 \mu\text{m}$) but with different disk diameters. (a) S1 with $d = 2.08 \mu\text{m}$ resonates at 3470 cm^{-1} and 1484 cm^{-1} . (b) S2 with $d = 2.21 \mu\text{m}$ resonates at 3360 cm^{-1} and 1410 cm^{-1} . (c) S3 with $d = 2.32 \mu\text{m}$ resonates at 3280 cm^{-1} and 1370 cm^{-1} . (d) S4 with $d = 2.43 \mu\text{m}$ exhibits two resonances at 3220 cm^{-1} and 1326 cm^{-1} . (e) S5 with $d = 2.55 \mu\text{m}$ reveals two resonances at 3044 cm^{-1} and 1280 cm^{-1} . The inset in panel (a) displays a photo of a $1 \times 1 \text{ cm}^2$ fabricated S1. The scale bars in all the SEM images correspond to $5 \mu\text{m}$.

electric field polarization is varied in the range of $0^\circ - 90^\circ$, which means that the DPA is highly efficient for practical applications such as thermal management as well as IR spectroscopic devices utilizing unpolarized light sources (random polarization). It is worth noting that the absorptivities of the fabricated DPAs shown in Fig. 2 were obtained with an unpolarized IR source and without the use of any polarizer.

Dual-band SEIRA study on DPA

As stated above, the DPAs' resonances cover a wide range of molecular vibrations. Here we exemplify its dual-band SEIRA spectroscopic capability by measuring 10-nm thin polydimethylsiloxane (PDMS) films, simultaneously targeting the CH_3 asymmetric C-H stretching at 2962 cm^{-1} and the CH_3 deformation in Si- CH_3 at 1263 cm^{-1} . Prior to the SEIRA study, a spectroscopic ellipsometry measurement on the PDMS film was also performed to verify the optical properties of the PDMS thin film, particularly the vibrations of the PDMS molecules; the details of this measurement are described in the Methods section. The full-range spectroscopic ellipsometry measurement and the fitting model results as well as the retrieved permittivity of the PDMS film, from the UV (50000 cm^{-1}) to the MIR (400 cm^{-1}) are

plotted in Fig. S5†. The measured permittivity data for PDMS is provided in Tab. S1†. As seen in Fig. S5†, while the PDMS film is almost transparent in the VIS – MIR region, many absorption features appear in the MIR region due to the vibrations of the PDMS film, including the asymmetric C-H stretching in CH_3 featuring at 2962 cm^{-1} and the CH_3 deformation in Si- CH_3 featured at 1263 cm^{-1} . To the best of our knowledge, this is the first systematic spectroscopic ellipsometry measurement for PDMS. The experiment was carried out over a wide spectral range, from the UV to the MIR region ($50000 \text{ cm}^{-1} - 400 \text{ cm}^{-1}$), providing a good quantitative reference for photonic and materials research. We also used ellipsometry to control the thickness of the PDMS film, which is linearly proportional to the concentration (volume ratio) of the PDMS dissolved in *n*-heptane solvent (the inset in Fig. S5b†).

The measured complex permittivity of PDMS focusing on the two different vibrations at 2962 cm^{-1} (CH_3) and at 1263 cm^{-1} (Si- CH_3) is plotted in Fig. 3a (real part) and Fig. 3b (imaginary part) for our SEIRA study. Fig. 3c and Fig. 3d show simulated and measured absorptivity spectra of a 10-nm PDMS film coated on DPA-S5. The two vibrational bands of PDMS at 2962 cm^{-1} and 1263 cm^{-1} are perfectly matched to the M1 and M2 resonant modes, respectively of S5. It is apparent that the two vibrations of PDMS are enhanced and coupled to the

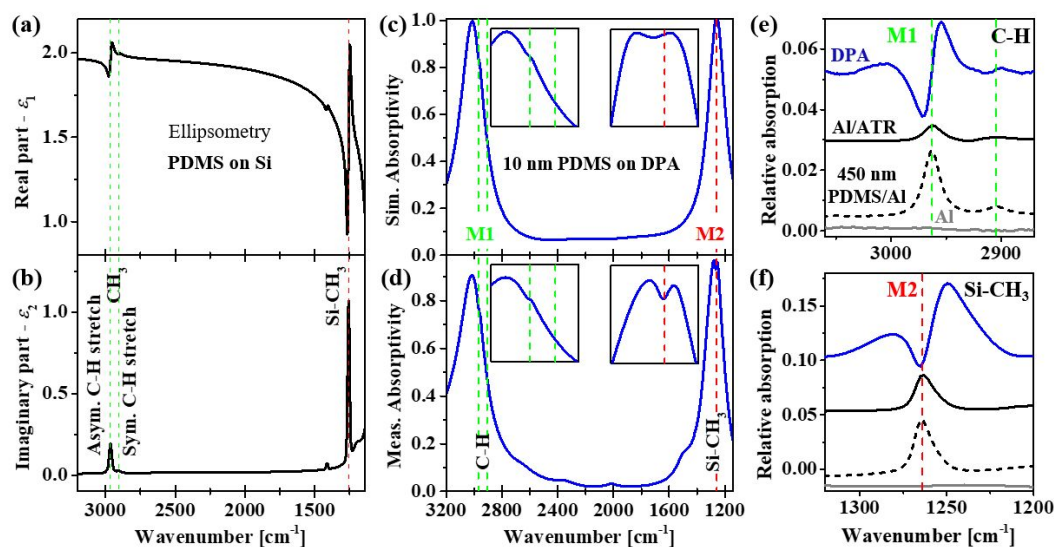


Fig. 3. (a) Real part and (b) imaginary part of the retrieved complex permittivity of PDMS in the MIR region focusing on two vibrations at 2962 cm^{-1} (asymmetric C-H stretching in CH_3) and 1263 cm^{-1} (CH_3 deformation in Si-CH_3). The full complex permittivity of PDMS is provided in Fig. S4[†]. (c) Simulated and (d) measured SEIRA spectra of 10-nm PDMS film coated on DPA-S5 reveal simultaneous detection of the two vibrations of PDMS (2962 cm^{-1} and 1263 cm^{-1}). Relative absorption SEIRA spectra of the 10-nm PDMS film coated on DPA-S5 (blue) and coated on 100-nm Al film measured by conventional reflection FTIR at normal incidence (grey) and at ATR (black) geometries: (e) at 2962 cm^{-1} (asymmetric C-H stretching in CH_3) and (f) at 1263 cm^{-1} (Si-CH_3). A shallow peak at 2904 cm^{-1} in (a) – (d) indicates the symmetric C-H stretching in CH_3 . Dashed black curves in (e) and (f) present relative absorption spectra of a 450-nm PDMS layer coated on 100-nm Al film measured in reflectance mode at normal incidence. Note that the signal from 10-nm PDMS layer coated on DPA-S5 is comparable to the signal from 450-nm PDMS on a planar Al film.

two resonant bands of S5, resulting in Fano-like absorption spectra. Since the presence of PDMS caused a redshift of the resonance of the DPA, a polynomial fitting procedure for each resonant band that is truncated at the vibration of PDMS was used as the reference for the subtraction to extract the enhanced spectra (relative absorption) of the PDMS vibrations. The relative absorption spectra at 2962 cm^{-1} (CH_3) and 1263 cm^{-1} (Si-CH_3) of the PDMS vibrations are plotted in Fig. 3e and Fig. 3f, respectively. For comparison, two FTIR spectra of a 10-nm PDMS film coated on a 100-nm sputtered Al film measured using the same reflectance setup at normal incidence as well as separately employing a sensitive attenuated total reflectance (ATR) geometry are also displayed. As shown in Fig. 3e and Fig. 3f, we do not observe any signals of CH_3 and Si-CH_3 vibrations from this 10-nm-PDMS-coated Al film via the reflectance geometry at normal incidence, but they are clearly observed by the ATR geometry, with the relative absorption intensities of 0.005 at the 2962 cm^{-1} and 0.025 at the 1263 cm^{-1} . In DPA-S5, these two vibrational signals are remarkably enhanced and simultaneously observed with the relative intensities of 0.03 (at 2962 cm^{-1}) and 0.08 (at 1263 cm^{-1}). These signal intensities are 3 – 5 times higher than those of the 10-nm-PDMS-coated Al film obtained using the ATR geometry, indicating that the DPA could be a sensitive antenna platform for multi-band SEIRA spectroscopy for the molecular fingerprint sensing. For a quantitative estimation of the SEIRA enhancement, the FTIR spectrum of a thick 450-nm PDMS layer coated on a 100-nm Al film substrate was also obtained using the same reflectance setup; the absorption intensities of both the C-H stretching and Si-CH_3 vibrations are almost

comparable to those of the 10-nm PDMS layer coated on DPA-S5. From the Beer–Lambert law and considering the molecules those who contribute to the SEIRA signal (10-nm PDMS coated on DPA-S5) and bulk PDMS vibration (450-nm PDMS film coated on Al film) intensities, the SEIRA enhancement factor of the DPA can be expressed as: $EF = \frac{I_{SEIRA}}{I_{bulk}} \frac{N_{bulk}}{N_{SEIRA}}$ (see ESI[†] for details). Here I_{SEIRA} and I_{bulk} are intensities of the molecular vibration mode from a 10-nm PDMS layer coated on DPA-S5 (SEIRA) and from a 450-nm PDMS film coated on the plain Al film, respectively. N_{bulk} and N_{SEIRA} are the number of PDMS molecules contributed to vibrational signals of a 450-nm PDMS film coated on Al film and the SEIRA signal on DPA-S5, respectively (see the ESI[†] and Fig. S6[†] for the detailed derivation). Herein the enhancement factors were found to be as high as 571 at M1 and 642 at M2. These values mean that the DPA could be able to overcome the detection limit of the conventional normal incidence reflectance and ATR measurements together with its excellent mode selectivity.

Real-time monitoring of PDMS formation

In addition to identifying the chemical bonds within a molecule by means of its vibrational absorption spectrum, *in situ* IR spectroscopy can be used to monitor the real-time reaction process^{44,45}. In this context, we studied the critical behaviour of crosslinking polymers by extending our “bond-selective” SEIRA technique using DPA antennas for the real-time monitoring of the reaction kinetics and gelation

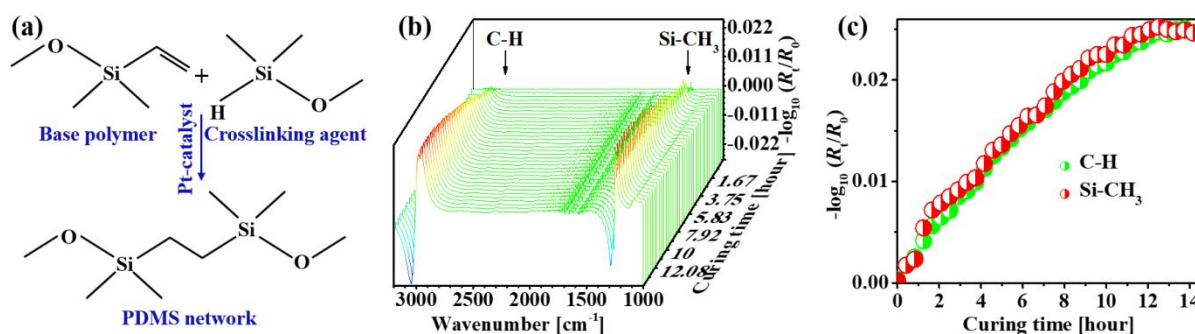


Fig. 4. (a) Hydrosilylation reaction of PDMS. (b) Bond-selective *in situ* SEIRA spectroscopy recorded during the curing time of 10-nm PDMS film coated on device S5. (c) The evolution of the SEIRA absorption intensity of both C-H (half-filled green circles) and Si-CH₃ (half-filled red circles) vibrations as a function of the curing time.

process from a 10-nm PDMS elastomer. A 10-nm film of a precursor mixture of the PDMS elastomer film was prepared on DPA-S5 at room temperature. Subsequently, the as-prepared PDMS elastomer film was continuously cured during which time the curing process was monitored by observing changes in the C-H stretching and CH₃ deformation signals enhanced by DPA-S5. In this *in situ* SEIRA spectroscopy, the initial reflectance (R_0) spectrum of the sample was used as the reference spectrum, and the change in the SEIRA reflectance (R_t/R_0) spectra was measured at 25-min intervals over a total time period of 15 h. Fig. 4a illustrates the hydrosilylation reaction of PDMS between the base polymer and crosslinking agent. Fig. 4b presents the IR spectral evolution ($-\log_{10}(R_t/R_0)$) as a function of curing time for the sample. As seen in Fig. 4b and Fig. 4c, the signal intensities of both the C-H stretching and the CH₃ deformation modes remarkably increase as the curing time increases, and then they begin to saturate after approximately 10 h, which indicates that the PDMS elastomer is completely reacted after 10 h. It is worth noting that we did not observe any signal from a 10-nm thick PDMS film coated on a 100-nm Al flat film using the same reflectance geometry. Here we can consider that the IR absorbance change of the C-H stretching and the CH₃ deformation of the PDMS elastomer will be proportional to the percentage of the reacted bonds in PDMS, i.e., the local conformation change associated with the reduction of the crosslinker's S-H bond and C-Si bond formation during the hydrosilylation reaction (Fig. 4a)⁴⁴. This local conformational change accompanied with the hydrosilylation reaction inevitably induces local redistribution of the bond charge leading to the alteration in the dynamic dipoles of the C-H stretching and the CH₃ deformation modes. As observed, the enhanced vibrational signals of the C-H stretching and the CH₃ deformation were increased during the curing process and then saturated when the PDMS elastomer film was completely cured. Consequently, the number of the cured PDMS elastomer was proportional to the absorbances ($-\log_{10}(R_t/R_0)$) of the C-H stretching and the CH₃ deformation. Therefore, the conversions α can be predicted by the following equation (details are shown in the ESI[†] and Fig. S7[†]):

$$\alpha_t = \frac{\log_{10}(R_t/R_0)}{\log_{10}(R_s/R_0)}, \text{ where } R_s/R_0 \text{ is the saturated SEIRA reflectance}$$

(when the curing process completely finishes). Fig. S7[†] plots the degrees of the conversions at both C-H and Si-CH₃ vibrations as functions of the reaction times. The measured kinetics of the reaction can be expressed by the n^{th} -order model^{46,47}: $\frac{d\alpha}{dt} = K(1-\alpha)^n$ where $K = K_0 \exp\left(\frac{-E_a}{RT}\right)$ is the rate constant following the Arrhenius equation, K_0 is the Arrhenius frequency factor, E_a is the activation energy, R is the universal gas constant ($R = 8.314 \text{ J}\cdot\text{mol}^{-1}\cdot\text{K}^{-1}$), T is the absolute temperature ($T = 295 \text{ K}$), and t is the reaction time. By fitting the degrees of conversions using the above reaction rate equation, we obtained the Arrhenius frequency factor of 0.285 hour^{-1} , the activation energy of $2.074 \text{ kJ}\cdot\text{mol}^{-1}$ with the order $-n$ of the kinetic of 0.44 . It should be noted that both the C-H and the Si-CH₃ vibrations follow exactly the same kinetics indicating that the alteration in these two bonds are of the same chemical origin: in this case the cross-linking reaction and the network formation of PDMS elastomer. In addition, the DPA can also efficiently convert absorbed IR light into heat⁴⁸, which also enhances the curing process of PDMS elastomer. Thus, the DPA can be an efficient IR antenna platform to enhance the curing process of the polymer via light-to-heat conversion while it also enables monitoring the reaction kinetics and gelation process from a thin polymer film by plasmon-enhanced infrared spectroscopy.

Coupling between molecular vibrations and DPA's resonances

Furthermore, it is worth noticing that the coupling between the PDMS vibration and the DPA resonance results not only in the Fano-like resonance but also in a spectral shift of both the DPA resonance (besides a redshift caused by the higher refractive index of PDMS) and the PDMS vibration. The relative spectral-shift (redshift or blueshift) depends on the coupling strength of the PDMS vibration and the DPA resonance with respect to the overlapping between the molecular vibration and the absorber resonance (redshift for the lower energy side, blueshift for the higher energy side). It should be noted that our DPA antenna platform is designed to function at normal incidence as the SPP-coupled (third-order) magnetic resonance M1 works within a small incident angle range ($0^\circ - 15^\circ$), even though the fundamental magnetic mode M2 is slightly shifted to higher wavenumbers when the angle varies between 0° to 85° .

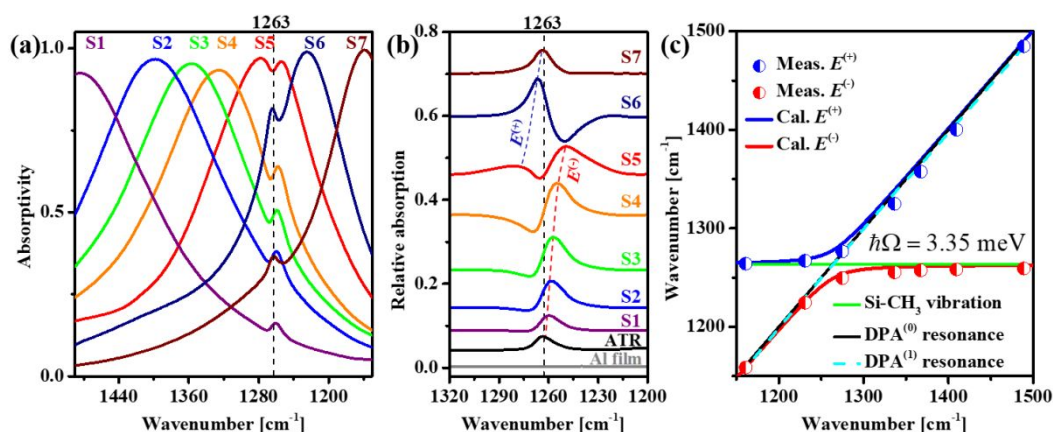


Fig. 5. (a) SEIRA spectra at around M2 mode of the 10-nm PDMS film coated on a set of DPAs (S1 – S5 with 3.0 μm periodicity and S6 – S7 with 4.4 μm periodicity) with resonances near the Si-CH₃ vibration of the PDMS molecule. (b) Relative SEIRA spectra of the Si-CH₃ vibration taken from the 10-nm PDMS films coated on DPAs, and on Al film measured by conventional reflectance and ATR geometries. (c) Hybridized modes (half-filled circles) resulted from the coupling between the Si-CH₃ vibration and the DPAs resonances plotted against the bare DPAs resonances (black line with slope = 1) and Si-CH₃ vibration at 1263 cm^{-1} (green line). The dashed cyan line denotes the DPAs resonances with the presence of the PDMS film. Blue and red lines plot the calculated hybridized modes.

The numerical simulation is shown in Fig. S2a[†], and the angle-resolved absorptivity measurement is shown in Fig. S8a[†] and Fig. S8b[†]. Here we also performed the angle-resolved SEIRA study of a 10-nm PDMS film coated on DPA-S5. Fig. S8c[†] presents the measured angle-resolved SEIRA spectra at the magnetic resonance – M2. As the indent angle increases, both the magnetic resonance M2 and the coupled Si-CH₃ vibrations are blue-shifted. To demonstrate the coupling strength between the PDMS vibrations and the DPA resonances, we performed a SEIRA study focusing on the PDMS vibrations (2962 cm^{-1} and 1263 cm^{-1}) using the five DPAs (S1 – S5) as well as two additional DPAs with the same periodicity and insulator thickness ($p = 4.4 \mu\text{m}$, $t = 0.2 \mu\text{m}$): S6 ($d = 2.97 \mu\text{m}$) and S7 ($d = 3.28 \mu\text{m}$). The details of S6 and S7 are described in the ESI[†] (Fig. S9[†]). The SEIRA spectra of the 10-nm PDMS-film-coated DPAs are plotted in Fig. 5a and the relative SEIRA intensities of the Si-CH₃ vibration are presented in Fig. 5b. It is clearly seen that the coupling strength between the Si-CH₃ vibration and the DPA resonance strongly depends on the overlap between the molecular vibration and the plasmon resonance. When the DPA resonance is close to the Si-CH₃ vibration, the molecular vibration intensity increases significantly. Compared to the original Si-CH₃ vibrational peak position (black line in Fig. 5b), the Si-CH₃ vibration is redshifted for samples S1 – S5 while it is blue-shifted for samples S6 and S7. Similarly, we also observed the spectral shift of the DPA resonances but in an opposite direction compared to the spectral shift of the molecular vibration (data not shown). In particular, we observed behaviour similar to Rabi splitting at the resonant peak of DPA-S5, in which the resonance is perfectly matched to the Si-CH₃ vibration (see red curve in Fig. 5a). SEIRA spectra of the asymmetric C-H stretching vibration were also examined for all the DPAs. The results are shown in Fig. S10a[†]. The relative absorption intensity of the asymmetric C-H stretching vibration gradually increases from S1 to S5 and from S7 to S6 as the spectral matching between the M1 resonance of the DPA and the C-H stretching vibration improves.

The hybridizations of the Si-CH₃ vibrations and the DPAs are plotted in Fig. 5c (half-filled circles) alongside the bare DPAs resonances (black line, denoted DPA⁽⁰⁾) and the original Si-CH₃ vibration (at 1263 cm^{-1} , green line). As discussed above, the higher refractive index of the PDMS leads to a redshift of the DPA resonance (optical shift) when the DPA is covered by a 10-nm film (denoted DPA⁽¹⁾), and the peak shift of the observed DPA resonance results from a combination of the optical shift and a shift due to coupling the molecular vibration–DPA plasmon coupling. To quantify the optical shift energy (denoted $\Delta\omega$) for each of the DPAs covered by a 10-nm PDMS film, we performed simulations using the lossless PDMS permittivity (the imaginary permittivity of PDMS was fixed at 0), for all seven DPAs with a conformal coating consisting of a 10-nm PDMS film. Thus, the energy of each DPA resonance after a redshift by a 10-nm PDMS film ($E_{\text{DPA}^{(1)}} = \hbar\omega_{\text{DPA}^{(1)}}$) can be calculated via the measured energy of DPA⁽⁰⁾ ($E_{\text{DPA}^{(0)}} = \hbar\omega_{\text{DPA}^{(0)}}$) and optical shifted energy ($\Delta\omega$) retrieved by simulation: $E_{\text{DPA}^{(1)}} = E_{\text{DPA}^{(0)}} - \Delta\omega$. The dashed cyan line shown in Fig. 5c plots the DPAs' resonances with optical shifts (DPA⁽¹⁾). To elucidate the coupling strength between the DPAs and the Si-CH₃ vibration of PDMS, we used a Hamiltonian that follows the Jaynes–Cummings model for the light-matter coupling system: $\hat{H} = \hat{H}_{\text{DPA}^{(1)}} + \hat{H}_{\text{Si-CH}_3} + \hat{H}_{\text{int}} = \hbar\omega_{\text{DPA}^{(1)}}\hat{a}^\dagger\hat{a} + \hbar\omega_{\text{Si-CH}_3}\hat{\sigma}^\dagger\hat{\sigma} + \hbar g(\hat{a}\hat{\sigma}^\dagger + \hat{a}^\dagger\hat{\sigma})$, where \hat{a} (\hat{a}^\dagger) and $\hat{\sigma}$ ($\hat{\sigma}^\dagger$) are the annihilation (creation) operators of the field (plasmon) and the optically active molecular vibration^{49–51}. The plasmon-vibration interaction g (coupling constant) is given as $g = \sqrt{\frac{\mu^2\omega_{\text{Si-CH}_3}}{2\hbar V\epsilon_0\epsilon}}$, where μ is the molecular dipole moment, V is the effective mode volume of the plasmon, ϵ_0 is the vacuum permittivity and ϵ is the effective dielectric constant of PDMS near the DPA surface. It is worth noting that, compared with the Fabry–Perot microcavity, plasmonic absorbers can exhibit a high coupling

constant due to the extreme enhancement of the nearfield in the vicinity of the resonators, defining a small mode volume; this approach therefore provides a powerful platform for studying light-matter coupling.

Since the vibration-plasmon polariton-coupled system has only one vibration (Si-CH₃), the expression of the Hamiltonian can be

simplified as: $\hat{H} = \begin{pmatrix} E_{DPA^{(1)}} & \Delta E \\ \Delta E & E_{Si-CH_3} \end{pmatrix}$, where $\Delta E = \hbar g$ is the coupling

strength. Through the diagonalization of this matrix, the Hamiltonian yields energy eigenvalues of the two hybridized states:

$E^{(\pm)} = \frac{1}{2}(E_{DPA^{(1)}} + E_{Si-CH_3}) \pm \frac{1}{2}\sqrt{(E_{DPA^{(1)}} - E_{Si-CH_3})^2 + 4\Delta E^2}$ (plotted as blue

and red curves in Fig. 5c). The coupling strength can therefore be

calculated as $\Delta E = \frac{1}{2}\sqrt{(E^{(+)} - E^{(-)})^2 - (E_{DPA^{(1)}} - E_{Si-CH_3})^2}$. From the

measured hybridized states energy ($E^{(\pm)}$), the optically shifted DPA resonance energy ($E_{DPA^{(1)}}$), and the Si-CH₃ vibration energy (E_{Si-CH_3}),

the coupling strength (ΔE) was found to be 1.78 meV (14.32 cm⁻¹).

The splitting energy ($\hbar\Omega = 2\Delta E = 2\hbar g$) was also estimated to be as

high as 3.55 meV. Furthermore, the hybridization between the C-H

stretching vibration and the M1 resonance was also investigated for

all DPAs (Fig. S10b†). The coupling strength between the C-H

stretching and M1 was found to be 4.57 meV (36.85 cm⁻¹). The

relative coupling strength energy defined as the coupling strength

and vibrational energy ratio ($\Delta E/E$) was 0.012, which is almost

comparable to that of the coupling between the Si-CH₃ vibration and

the M2 resonance. Thus, this simple aluminum DPA structure could

be another interesting plasmonic antenna platform with a strong

field enhancement for the study of light-matter interactions such as

the vibration-plasmon polariton-coupled system demonstrated in

the present study. Although, the splitting energy in this vibration-

plasmon polariton in the MIR region is much smaller than that of

exciton-plasmon polaritons in UV-VIS region⁵²⁻⁵⁴, it is comparable to

the linewidth of the Si-CH₃ vibration (1.67 meV) as well as those

values for previously reported perfect absorbers made of gold loaded

with molecules²⁹. However, the splitting energy value is still far

below the bandwidth of the DPA resonance (i.e. 30 meV), indicating

that the coupling between DPA resonances and PDMS vibrations is in

the weak coupling regime.

Conclusions

We have demonstrated simple, single-sized aluminum disk arrays

fabricated by colloidal-mask lithography for dual-band, polarization-

independent plasmonic perfect absorbers for high-sensitivity

molecular sensing and *in situ* reaction monitoring also capable of

selective analysis of their reaction kinetics. The fabricated large-area

DPAs exhibited two narrow resonant bands with nearly perfect

absorptivities and high tunability in the IR region spanning the most

important vibrations of molecular spectroscopy. First, we have

demonstrated dual-band SEIRA spectroscopy for selectively

detecting two vibrational bands (asymmetric C-H stretching in CH₃ at

2962 cm⁻¹ and CH₃ deformation in Si-CH₃ at 1263 cm⁻¹) of a 10-nm PDMS film. Second, the DPA antenna platform revealed its outstanding applicability via real-time SEIRA observation of the curing and gelation kinetics of the ultrathin PDMS film. Finally, the effects of hybridization between the DPAs resonances and the PDMS vibrations were also studied quantitatively as evidenced by the emergence of avoided-crossings for the polaritonic bands. Overall, the proposed plasmonic DPAs fabricated by the scalable colloidal-mask lithography provide a good plasmonic antenna platform not only for IR molecular and reaction sensors but can also be effectively adopted for gas sensors and thermal imaging, as well as many other light-matter polaritonic applications from the VIS to the THz regions.

Methods section

Fabrication of DPAs. The DPAs were fabricated using colloidal-mask

lithography combined with a two-step RIE process. For each DPA, a

tri-layered Al/Al₂O₃/Al film was deposited on a 1×1 cm² Si (100)

substrate using three sputtering steps (i-Miller CFS-4EP-LL, Shibaura).

To prepare the Al disk array on the Al₂O₃/Al film, a monolayer of

polystyrene (PS) spheres (Polybead Polystyrene Microspheres –

Polysciences; the standard deviations: 0.07 μm for 3.0 μm PS and

0.015 μm for 4.4 μm PS) was deposited on top of each tri-layer film

as an RIE mask. To reduce the size of the PS spheres, the oxygen

plasma etching with an etching rate of 2 nm/s (20-sccm O₂ gas, 1-Pa

APC pressure, 200-W RF antenna power, 5-W RF bias power, ULVAC

CE-300I) was applied. Here, a short 90-s burst of RIE was repeated on

each sample to prevent overheating by the ion bombardment. The

etching time on each sample was precisely controlled to achieve

different PS sizes corresponding to the designed Al-disk sizes. Then,

a second RIE step was applied to etch Al with PS mask (a mixture of

3-sccm BCl₃ and 3-sccm Cl₂ gases, 0.15-Pa APC pressure, 50 W RF

antenna power, 10-W RF bias power, and an etching rate of 0.82

nm/s) forming Al disk array. DPAs were finally achieved by removing

the PS mask in toluene and ethanol. We note that the size of the Al

disk was principally determined by the etching time of the PS

spheres.

Characterizations. SEM images of the fabricated DPAs were obtained

using a Hitachi SU8200 SEM system under an accelerating voltage of

5 kV. The reflectance spectra were obtained using an FTIR

spectrometer (Nicolet iS50R FT-IR Thermo Scientific) equipped with

a variable-angle reflectance compartment accessory and a liquid-

nitrogen-cooled mercury cadmium telluride (MCT) detector

combined with a KBr beam splitter. For ATR measurement of the 10-

nm PDMS coated Al film, an ATR accessory (iS50 ATR) equipped with

a deuterated triglycine sulfate detector (DTGS) detector and KBr

beam splitter was employed. A 200-nm Au film was used as the

reference for all the measurements. The absorptivity spectra of the

fabricated devices were simply calculated as 1 – reflectance (the Al

film at the base of the samples blocked any transmitted light in the

MIR region, so transmittance = 0). The spectroscopic ellipsometry

study of the PDMS film was carried out using two ellipsometers

(SENTECH, SE 850 DUV for UV – NIR region and SENDIRA for MIR

region). Further details of the spectroscopic ellipsometry and analysis are provided in the ESI[†].

Simulations. The optical spectra (transmittance, reflectance, and absorptivity) of the DPAs were calculated using the rigorous coupled-wave analysis (RCWA) (DiffractMOD, Synopsys' RSoft). For the electric and magnetic field distributions, full-wave simulations based on the finite-difference time-domain (FDTD) method (FullWAVE, Synopsys' RSoft) were performed. The dielectric functions of Al, Al₂O₃ and Si were obtained in the literature⁵⁵, and the dielectric function of PDMS was measured via spectroscopic ellipsometry. The modelling of the DPA was performed in a CAD layout (RSoft CAD) with the unit cell as shown in Fig. 1a, and with the mesh size of 20 nm (2 nm for the PDMS layer in the SEIRA study). For the FDTD simulations, periodic boundary conditions were applied to both the X- and Y-directions and perfectly matched layers were applied to both directions of the Z-axis. For both RCWA and FDTD simulations, the excitation electromagnetic field propagated along the -Z-direction (at normal incidence except in the case of the angle dependence simulation shown in Fig. S2a[†]) and the electric field oscillated along in the X-axis (except the polarization dependence simulation). The reflectance, transmittance and absorptivity spectra were taken at the same incident angle.

Conflicts of interest

The authors declare no competing financial interest.

Acknowledgements

This work is partially supported by JSPS KAKENHI (16F16315, JP16H06364, 16H03820), and CREST "Phase Interface Science for Highly Efficient Energy Utilization" (JPMJCR13C3) from Japan Science and Technology Agency. Thang. D. Dao acknowledges the JSPS fellowship program (P16315).

References

- N. I. Landy, S. Sajuyigbe, J. J. Mock, D. R. Smith and W. J. Padilla, *Phys. Rev. Lett.*, 2008, **100**, 207402.
- M.-W. Tsai, T.-H. Chuang, C.-Y. Meng, Y.-T. Chang and S.-C. Lee, *Appl. Phys. Lett.*, 2006, **89**, 173116.
- H. T. Miyazaki, K. Ikeda, T. Kasaya, K. Yamamoto, Y. Inoue, K. Fujimura, T. Kanakugi, M. Okada, K. Hatade and S. Kitagawa, *Appl. Phys. Lett.*, 2008, **92**, 141114.
- Y.-H. Ye, Y.-W. Jiang, M.-W. Tsai, Y.-T. Chang, C.-Y. Chen, D.-C. Tzuang, Y.-T. Wu and S.-C. Lee, *Appl. Phys. Lett.*, 2008, **93**, 033113.
- X. Liu, T. Tyler, T. Starr, A. F. Starr, N. M. Jokerst and W. J. Padilla, *Phys. Rev. Lett.*, 2011, **107**, 045901.
- T. D. Dao, K. Chen, S. Ishii, A. Ohi, T. Nabatame, M. Kitajima and T. Nagao, *ACS Photonics*, 2015, **2**, 964–970.
- T. Yokoyama, T. D. Dao, K. Chen, S. Ishii, R. P. Sugavaneshwar, M. Kitajima and T. Nagao, *Adv. Opt. Mater.*, 2016, **4**, 1987–1992.
- F. B. P. Niesler, J. K. Gansel, S. Fischbach and M. Wegener, *Appl. Phys. Lett.*, 2012, **100**, 203508.
- S. Ogawa, K. Okada, N. Fukushima and M. Kimata, *Appl. Phys. Lett.*, 2012, **100**, 021111.
- F. Zhao, C. Zhang, H. Chang and X. Hu, *Plasmonics*, 2014, **9**, 1397–1400.
- S. Ogawa, D. Fujisawa, H. Hata, M. Uetsuki, K. Misaki and M. Kimata, *Appl. Phys. Lett.*, 2015, **106**, 041105.
- T. D. Dao, S. Ishii, T. Yokoyama, T. Sawada, R. P. Sugavaneshwar, K. Chen, Y. Wada, T. Nabatame and T. Nagao, *ACS Photonics*, 2016, **3**, 1271–1278.
- J. Y. Suen, K. Fan, J. Montoya, C. Bingham, V. Stenger, S. Sriram and W. J. Padilla, *Optica*, 2017, **4**, 276.
- H. T. Miyazaki, T. Kasaya, M. Iwanaga, B. Choi, Y. Sugimoto and K. Sakoda, *Appl. Phys. Lett.*, 2014, **105**, 121107.
- A. Lochbaum, Y. Fedoryshyn, A. Dorodnyy, U. Koch, C. Hafner and J. Leuthold, *ACS Photonics*, 2017, **4**, 1371–1380.
- E. Rephaeli and S. Fan, *Opt Express*, 2009, **17**, 15145–15159.
- L. P. Wang and Z. M. Zhang, *Appl. Phys. Lett.*, 2012, **100**, 063902.
- B. Zhao, L. Wang, Y. Shuai and Z. M. Zhang, *Int. J. Heat Mass Transf.*, 2013, **67**, 637–645.
- J.-Y. Chang, Y. Yang and L. Wang, *Int. J. Heat Mass Transf.*, 2015, **87**, 237–247.
- E. Rephaeli, A. Raman and S. Fan, *Nano Lett.*, 2013, **13**, 1457–1461.
- A. P. Raman, M. A. Anoma, L. Zhu, E. Rephaeli and S. Fan, *Nature*, 2014, **515**, 540–544.
- L. Zhu, A. Raman, K. X. Wang, M. A. Anoma and S. Fan, *Optica*, 2014, **1**, 32.
- T. Liu and J. Takahara, *Opt. Express*, 2017, **25**, A612.
- A. Hartstein, J. R. Kirtley and J. C. Tsang, *Phys. Rev. Lett.*, 1980, **45**, 201–204.
- D. Enders, T. Nagao, T. Nakayama and M. Aono, *Langmuir*, 2007, **23**, 6119–6125.
- F. Neubrech, A. Pucci, T. W. Cornelius, S. Karim, A. García-Etxarri and J. Aizpurua, *Phys. Rev. Lett.*, 2008, **101**, 157403.
- D. Enders, T. Nagao, A. Pucci, T. Nakayama and M. Aono, *Phys. Chem. Chem. Phys.*, 2011, **13**, 4935–4941.
- T. Nagao, G. Han, C. V. Hoang, J.-S. Wi, A. Pucci, D. Weber, F. Neubrech, V. M. Silkin and D. Enders, O. Saito and M. Rana, *Sci. Technol. Adv. Mater.*, 2010, **11**, 054506.
- K. Chen, R. Adato and H. Altug, *ACS Nano*, 2012, **6**, 7998–8006.
- C. V. Hoang, M. Oyama, O. Saito, M. Aono and T. Nagao, *Sci. Rep.*, 2013, **3**, 1175.
- K. Chen, T. D. Dao, S. Ishii, M. Aono and T. Nagao, *Adv. Funct. Mater.*, 2015, **25**, 6637–6643.
- A. E. Cetin, S. Korkmaz, H. Durmaz, E. Aslan, S. Kaya, R. Paiella and M. Turkmen, *Adv. Opt. Mater.*, 2016, **4**, 1274–1280.
- Mayerhöfer Thomas G. and Popp Jürgen, *Nanophotonics*, 2018, **7**, 39.
- Z. H. Jiang, S. Yun, F. Toor, D. H. Werner and T. S. Mayer, *ACS Nano*, 2011, **5**, 4641–4647.
- H. Cheng, S. Chen, H. Yang, J. Li, X. An, C. Gu and J. Tian, *J. Opt.*, 2012, **14**, 085102.
- B. Zhang, Y. Zhao, Q. Hao, B. Kiraly, I.-C. Khoo, S. Chen and T. J. Huang, *Opt. Express*, 2011, **19**, 15221–15228.
- C. Koechlin, P. Bouchon, F. Pardo, J.-L. Pelouard and R. Haïdar, *Opt. Express*, 2013, **21**, 7025–7032.
- R. Feng, W. Ding, L. Liu, L. Chen, J. Qiu and G. Chen, *Opt. Express*, 2014, **22**, A335.
- N. Zhang, P. Zhou, D. Cheng, X. Weng, J. Xie and L. Deng, *Opt. Lett.*, 2013, **38**, 1125–1127.
- K. Ito, H. Toshiyoshi and H. Iizuka, *J. Appl. Phys.*, 2016, **119**, 063101.
- M. Pu, C. Hu, M. Wang, C. Huang, Z. Zhao, C. Wang, Q. Feng and X. Luo, *Opt Express*, 2011, **19**, 17413–17420.
- Y. J. Yoo, Y. J. Kim, P. Van Tuong, J. Y. Rhee, K. W. Kim, W. H. Jang, Y. H. Kim, H. Cheong and Y. Lee, *Opt. Express*, 2013, **21**, 32484.
- Y. Chen, J. Dai, M. Yan and M. Qiu, *Opt. Express*, 2014, **22**, 30807.
- S. K. Venkataraman, L. Coyne, F. Chambon, M. Gottlieb and H. H. Winter, *Polymer*, 1989, **30**, 2222–2226.
- J. E. Dietz, B. J. Elliott and N. A. Peppas, *Macromolecules*, 1995, **28**, 5163–5166.

ARTICLE

Journal Name

- 46 G. Liang and K. Chandrashekhara, *J. Appl. Polym. Sci.*, 2006, **102**, 3168–3180.
- 47 A. K. Burnham and L. N. Dinh, *J. Therm. Anal. Calorim.*, 2007, **89**, 479–490.
- 48 J. Hao, L. Zhou and M. Qiu, *Phys. Rev. B*, 2011, **83**, 165107.
- 49 E. T. Jeynes and F. W. Cummings, *Proc. IEEE*, 1963, **51**, 89–109.
- 50 J. del Pino, J. Feist and F. J. Garcia-Vidal, *New J. Phys.*, 2015, **17**, 053040.
- 51 W. Ahn, I. Vurgaftman, A. D. Dunkelberger, J. C. Owrutsky and B. S. Simpkins, *ACS Photonics*, 2018, **5**, 158–166.
- 52 G. Khitrova, H. M. Gibbs, M. Kira, S. W. Koch and A. Scherer, *Nat. Phys.*, 2006, **2**, 81.
- 53 S. Savasta, R. Saija, A. Ridolfo, O. Di Stefano, P. Denti and F. Borghese, *ACS Nano*, 2010, **4**, 6369–6376.
- 54 D. G. Baranov, M. Wersäll, J. Cuadra, T. J. Antosiewicz and T. Shegai, *ACS Photonics*, 2018, **5**, 24–42.
- 55 E. D. Palik, *Handbook of Optical Constants of Solids*, Academic Press: New York, 3rd edn., 1998.

Dual-band in situ molecular spectroscopy using single-sized Al-disk perfect absorbers

Thang Duy Dao*^a, Kai Chen^{ab}, Tadaaki Nagao*^{ac}

^aInternational Center for Materials Nanoarchitectonics, National Institute for Materials Science (NIMS), 1-1 Namiki, Tsukuba, Ibaraki 305-0044, Japan.

^bInstitute of Photonics Technology, Jinan University, Guangzhou, 510632, China

^cDepartment of Condensed Matter Physics, Graduate School of Science, Hokkaido University, Kita 8, Nishi 5, Kita-ku, Sapporo 060-0810, Japan

*Corresponding Authors: Dao.Duythang@nims.go.jp, NAGAO.Tadaaki@nims.go.jp

Table of content. Plasmonic perfect absorber with single-sized resonator for simultaneous sensitive dual-band vibrational sensing and real-time observation of molecular reaction kinetics

